Pre-deployment performance assessment of device-free radio localization systems

Conference Paper · May 2016

DOI: 10.1109/ICCW.2016.7503754

4 authors, including:

Sanaz Kianoush
University of Pavia
10 PUBLICATIONS **9** CITATIONS
SEE PROFILE

Vittorio Rampa
Italian National Research Council
61 PUBLICATIONS **329** CITATIONS
SEE PROFILE

Stefano Savazzi
Italian National Research Council
72 PUBLICATIONS **770** CITATIONS
SEE PROFILE

Copyright notice

It has been published in the Proceedings of the IEEE International Conference on Communications Workshops 2016 (ICC'2016), pp. 1-6, 23-27 May 2016, Kuala Lumpur, Malaysia, DOI: 10.1109/ICCW.2016.7503754.

Pre-deployment performance assessment of device-free radio localization systems

Sanaz Kianoush[1], Vittorio Rampa[1], Stefano Savazzi[1], Monica Nicoli[2]
[1]Institute of Electronics, Computer and Telecommunication Engineering (IEIIT), CNR
[2]Dipartimento di Elettronica, Informazione e Bioingegneria (DEIB), Politecnico di Milano
{sanaz.kianoush, vittorio.rampa, stefano.savazzi}@ieiit.cnr.it, monica.nicoli@polimi.it

***Abstract*—Device-free localization (DFL) systems have emerged in the last years as a powerful technology for tracking mobile targets without the need of radio tags. Perturbations induced by moving objects on the electromagnetic (EM) wavefield generated by a dense wireless network are measured and processed by the DFL system to track target trajectories. Despite several solutions have been explored in the literature, mainly based on fingerprinting approaches, a deep understanding of body-induced effects on the EM fields for target tracking is still missing as well as reliable predictive models for pre-deployment accuracy assessment of DFL systems. The paper makes a first attempt towards the definition and validation of a novel predictive tool that is general enough to be applied to DFL systems with any kind of RF interface, network topology and connectivity degree. An analytical diffraction model is exploited to predict the effect of a human body on the received signal strength field over all the available links and compute fundamental limits to the DFL positioning accuracy. The proposed tool is tailored for 2D human body localization and validated by experimental trials in an indoor environment.**

***Index Terms*—Device Free radio localization, Cramer-Rao lower bound, wireless sensor networks, Internet of Things.**

I. Introduction

Recent research has shown the electromagnetic (EM) field adopted for data transmission can be also used as a powerful sensing tool for device-free environmental vision [1] [2], [3]. Perturbations induced on radio-frequency (RF) signals can be measured and processed to extract an image of the environment that caused the perturbation. Each wireless link can thus act as a virtual sensor, while the combination of multiple, possibly heterogeneous, links enables an accurate understanding of human body motions. RF-based device-free localization (DFL) [2], [3] has therefore emerged as an attractive technology in several applications such as ambient assisted living [1], human sensing in industrial workspaces [4], [5], and infrastructure security systems [6]–[9].

DFL systems monitor the changes in the received signal strength (RSS) field originated by a wireless network, with the goal of locating and tracking targets (typically human bodies) without requiring them to carry any electronic device. A crucial problem for quantitative evaluation of the location accuracy is the availability of realistic but simple models to describe human-body induced shadowing of the RF field [10]. Ray-tracing [11], stochastic [12], [13], and geometric-based [3] models have been investigated to predict the relationship between human body position and the corresponding induced RSS perturbations. EM methods, that exploit geometric/uniform theory of diffraction (GTD/UTD), and ray-tracing algorithms as well, can be employed for their ability to accurately evaluate the EM field at the receiver. However, they are usually very complex, time consuming and, above all, require perfect knowledge of the shape, composition and EM properties of the target. In [14], a simplified but effective analytic framework, based on the Fresnel-Kirchoff diffraction theory, was considered to model target-induced RSS changes in line-of-sight (LOS) and non-LOS (NLOS) scenarios. Preliminary results on a single-link and two cross links deployments showed a good match between analytical and experimental data.

In this paper, we exploit the results in [14] to develop and validate a general tool for prediction of the location accuracy of a generic DFL system, accounting for arbitrary node deployment and network connectivity. The proposed analytical tool not only allows to predict the RSS sensitivity of each radio link to body movements, but it is also able to combine multiple links with any geometric arrangement for predictive performance analysis over the whole monitored area. It can be used for assessment of DFL performances before on-site deployment, or also to predict localization accuracy that can be achieved by an already deployed wireless network (*e.g.,* for communication purposes) before installing the DFL-enabled software for positioning.

An illustrative example to introduce the key features of the proposed tool is shown in Fig. 1: a target can freely move in an area covered by a device-to-device wireless network with pre-defined deployment and connectivity graph. The predicted location performance can be evaluated according to the Cramer-Rao Lower Bound (CRLB) for any target location before a real network setup as shown in the figure. This image highlights both coverage and accuracy performances of the DFL system. The coverage area is the zone where the target affects the RSS wavefield of the wireless links, *i.e.,* the superposition of the sensitivity areas [14] of all co-located links. The accuracy image highlights the predicted

This work has been partially supported by the project Mobilità Intelligente Ecosostenibile (MIE), funded by MIUR, within the framework Cluster Tecnologico Nazionale "Tecnologie per le Smart Communities".

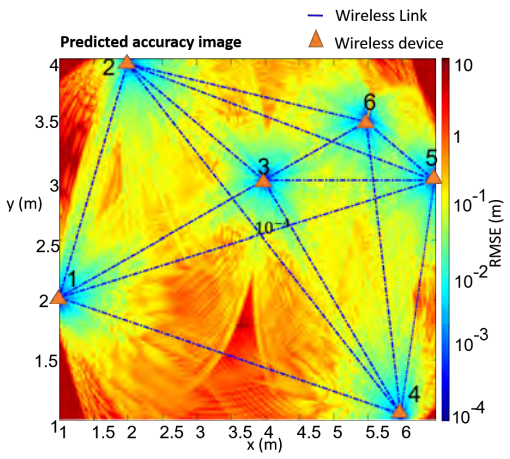

Fig. 1. Location accuracy predicted by the diffraction model vs. the target position (x, y) for a peer-to-peer network with full connectivity and node deployment as indicated in the superimposed image.

DFL performance for all possible positions (x, y) of the target in the coverage area, and identifies possibly critical scenarios (*i.e.,* positions characterized by low accuracy or partial coverage). To validate the proposed approach, a real positioning system, that employs IEEE 802.15.4 devices with customized DFL software, has been deployed and tested in a large indoor hall. Experimental data have been collected to compare the root mean square error (RMSE) performance of the DFL system with the predicted accuracy evaluated by the proposed analytical tool.

The paper is organized as follows: DFL system is described in Sect. II. Physical modeling of RSS for DFL systems is introduced in Sect. III, while accuracy bounds are investigated in Sect. IV. Predictive analysis and validation are described in Sect. V, and concluding remarks are presented in Sect. VI.

II. Device-free localization model

We consider a DFL scenario with a single human target that moves within a monitored area $\mathcal{X}$. A wireless network of N devices is deployed over the area according to an arbitrarily complex layout, as shown in Fig. 1. The nodes perform synchronous RSS measurements over $L \leq N(N-1)/2$ peer-to-peer links and forward the data to a gateway node which serves as network coordinator (NC) and processing unit [13]. Let $\mathbf{s}_t = [s_{1,t} \cdots s_{L,t}]^T$ be the noisy power measurements collected by the NC at discrete time instants $t = 1, 2, \ldots$, where each observation $s_{\ell,t}$ represents the RSS measured (in dB scale) over the link $\ell \in \mathcal{L} = \{1, \ldots, L\}$ during the t-th time interval. The aim of the DFL system is to estimate the 2D target position $\mathbf{x}_t = [x_t, y_t]^T$ within the area $\mathcal{X}$ using the measurements $\mathbf{s}_t$ at each time t.

Stochastic modeling is adopted to relate the perturbations of the RSS wavefield to the target position $\mathbf{x}_t$. Since the target presence affects both attenuation and random fluctuations of the received power, a log-normal power model [15] is defined where the RSS mean and variance are expressed as functions of the target location. Specifically, $\forall \ell \in \mathcal{L}$, the RSS $s_{\ell,t}$ is modeled as a Gaussian random variable with statistics that depend on the absence (*i.e.,* $\mathbf{x}_t \notin \mathcal{X}_\ell$) or presence (*i.e.,* $\mathbf{x}_t = \mathbf{x} \in \mathcal{X}_\ell$) of the target at location $\mathbf{x} = [x, y]^{\mathrm{T}}$ inside the sensing area $\mathcal{X}_\ell$ of the ℓ-th link, as [13]

$$s_{\ell,t} = \begin{cases} \mu_{\ell,0} + w_{\ell,0} & \text{if } \mathbf{x}_t \notin \mathcal{X}_\ell \\ \mu_\ell(\mathbf{x}) + w_\ell(\mathbf{x}) & \text{if } \mathbf{x}_t = \mathbf{x} \in \mathcal{X}_\ell. \end{cases} \quad (1)$$

As shown in Sect. III, the sensing area $\mathcal{X}_\ell$ refers to the zone around the LOS path of the ℓ-th link where the effect of the target is prominent. Depending on nodes deployment, the region of interest $\mathcal{X}$ may be covered by an arbitrary number of links with superimposed sensing areas $\mathcal{X}_\ell$, thus making localization more accurate in some positions (*i.e.,* belonging to areas covered by several links) and less accurate in others.

In the empty scenario case, *i.e.,* for $\mathbf{x}_t \notin \mathcal{X}_\ell$, the RSS has a deterministic mean $\mu_{\ell,0}$ that accounts for path-loss and static multipath effects, while $w_{\ell,0} \propto \mathcal{N}(0, \sigma^2_{\ell,0})$ models the random fluctuations due to measurement errors or small variations in the environment. According to (1), when the target is in the link sensitivity area, *i.e.,* for $\mathbf{x}_t = \mathbf{x} \in \mathcal{X}_\ell$, the received signal is subject to an increased fluctuation due to the random term $w_\ell(\mathbf{x}) \propto \mathcal{N}(0, \sigma^2_\ell(\mathbf{x}))$. The human-induced attenuation $\mu_\ell(\mathbf{x})$ and standard deviation $\sigma_\ell(\mathbf{x})$ are given by

$$\mu_\ell(\mathbf{x}) = \mu_{\ell,0} - \Delta\mu_\ell(\mathbf{x}) \quad (2)$$

$$\sigma_\ell(\mathbf{x}) = \sigma_{\ell,0} + \Delta\sigma_\ell(\mathbf{x}) \quad (3)$$

where $\Delta\mu_\ell(\mathbf{x})$ highlights the path-loss changes induced by the human body presence, while $\Delta\sigma_\ell(\mathbf{x}) \geq 0$ denotes the corresponding increase of RSS fading. Note that RSS observations are continuously sampled over a finite time interval (*e.g.,* 60 ms for system validation of Sect. V) that depends on the device duty-cycle. During this interval, the target can freely move, turn or change posture and position. The event $\mathbf{x}_t = \mathbf{x}$ here denotes the target being located in the surroundings of $\mathbf{x}$ assuming any orientation or posture.

For position estimation, both reference configuration $\{\mu_{\ell,0}, \sigma_{\ell,0}\}$, corresponding to the empty scenario, and the perturbation maps $\{\Delta\mu_\ell(\mathbf{x}), \Delta\sigma_\ell(\mathbf{x})\}$ for all positions $\mathbf{x} \in \mathcal{X}_\ell$, must be known for each link $\ell \in \mathcal{L}$. While $\{\mu_{\ell,0}, \sigma_{\ell,0}\}$ can be easily pre-calibrated when no target is moving in the network area, evaluation of the maps $\{\Delta\mu_\ell(\mathbf{x}), \Delta\sigma_\ell(\mathbf{x})\}$ is more time consuming as it requires extensive fingerprinting campaigns [8] or ray-tracing simulations [11]. The goal of the model detailed in Sect. III is twofold: to predict the effect of human body motions on RSS, simplifying the DFL calibration stage, and to enable pre-deployment prediction of the localization accuracy, based on the CRLB, herein defined in closed form for any position inside the monitored area.

III. Physical modeling of RSS for DFL systems

The RSS model described below highlights human-induced shadowing effects observed by the ℓ-th link,

whose geometrical properties (*i.e.,* link distance, transmitter/receiver height from ground) are herein assumed as known: it refers to a single 3D target that is placed across or near the LOS path connecting the transmitter (TX) and the receiver (RX) nodes. In Fig. 2, the 3D target is modeled as a 2D perfectly absorbing EM surface, also known as knife-edge [14], having the same height $2a_z$ and traversal size $2a_y$ of the 3D object. Both height $2a_z$ and traversal size $2a_y$ of the 2D knife-edge obstacle are referred to the barycenter $\mathbf{x}$ of the obstacle itself having coordinates $\mathbf{x} = (x, y, 0)$. In the following, the LOS link is supposed to be horizontally placed at distance h from the floor, while the target location is identified only by the coordinates $\mathbf{x}$ of the barycenter; for the sake of simplicity the constant coordinate z is dropped being $z = 0$.

We model the attenuation induced by the target according to the RSS values $\mu_\ell(\mathbf{x})$ and $\mu_{\ell,0}$ that are measured when the obstacle is present at position $\mathbf{x}$ and absent (*i.e.,* free-space or empty scenario), respectively. Attenuation prediction as a function of the target position $\mathbf{x}$ is based on the EM diffraction model [14] that is herein briefly reviewed. We assume that each link length d_ℓ is defined as $d_\ell = r_{T,\ell} + r_{R,\ell}$ where $r_{T,\ell}$ and $r_{R,\ell}$ are the distances of the obstacle from the TX and RX, respectively. Moreover, if the link distance from the floor (*i.e.,* h in Fig. 2), walls, ceiling or other furniture is greater than the Fresnel's radius $R_\ell = \sqrt{\lambda\, r_{T,\ell}\, r_{R,\ell}/d_\ell}$ and the multi-path effects due to these scenario elements are negligible, then only the target influences the received signal. λ is the wavelength of the transmitted signal.

Let the target be standing at a fixed position $\mathbf{x}$, under this simplifying setting, the attenuation $A_C = A_C(\mathbf{x}, a_y, a_z, d_\ell)$ induced by the obstacle can be defined as a function of $\mathbf{x}$ with known geometrical terms a_y, a_z and d_ℓ. Exploiting the diffraction model and the paraxial approximation [14], it is

$$A_C = \frac{1}{1 + (C_z^2 + S_z^2)(\Gamma_C^2 + \Gamma_S^2) - 2S_z\Gamma_C - 2C_z\Gamma_S} \quad (4)$$

where $C_z = C\left(\frac{a_z}{R_\ell/\sqrt{2}}\right)$, $S_z = S\left(\frac{a_z}{R_\ell/\sqrt{2}}\right)$, $\Gamma_C = C\left(\frac{y+a_y}{R_\ell/\sqrt{2}}\right) - C\left(\frac{y-a_y}{R_\ell/\sqrt{2}}\right)$ and $\Gamma_S = S\left(\frac{y+a_y}{R_\ell/\sqrt{2}}\right) - S\left(\frac{y-a_y}{R_\ell/\sqrt{2}}\right)$ refer to the Fresnel's Cosine $C(\cdot)$ and Sine $S(\cdot)$ functions. As the target moves away from the LOS path, it induces an attenuation that decreases and it is negligible outside the influence zone defined as $\mathcal{X}_\ell = \mathcal{X}_\ell(W_\ell, d_\ell) \triangleq \left\{\mathbf{x} \in \mathcal{X}_\ell(W_\ell, d_\ell) : 0 \le x \le d_\ell,\ |y| \le \frac{1}{2}\mathrm{W}_\ell\right\}$; if $a_z \gg R_\ell$, then $\mathrm{W}_\ell = \mathrm{W}_\ell(x)$ can be approximated as $\mathrm{W}_\ell \simeq R_\ell^2/a_y = \lambda x\,(d_\ell - x)/a_y d_\ell$ [14].

The predicted additional attenuation according to the diffraction model for an equivalent 2D knife-edge target is found in (4). However, as mentioned in Sect. II, the human body can move (*e.g.,* wandering, turning, etc.) in the surroundings of $\mathbf{x}$ during the observation time window. The true position $\mathbf{x} + \Delta\mathbf{x}$ of the obstacle can thus be modeled by a random deviation $\Delta\mathbf{x}$ inside a 2D bin of size $\Delta \times \Delta$ centered around $\mathbf{x}$; moreover, the target is also assumed

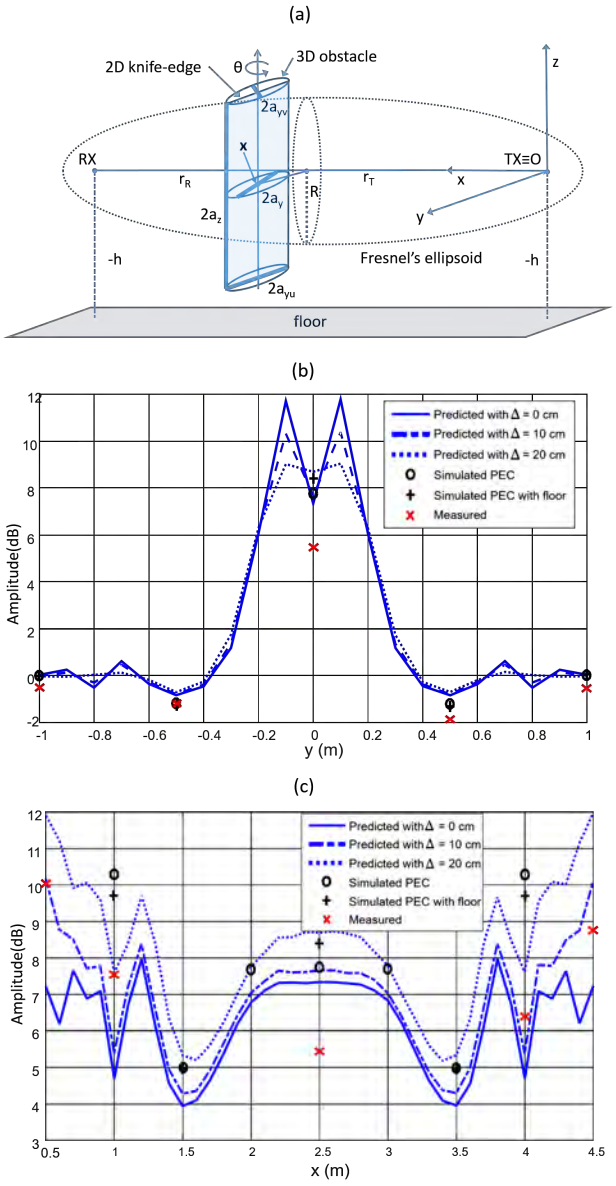

Fig. 2. RSS perturbation modeling: a) Sketch of the layout adopted to evaluate the influence of a 2D obstacle in a single-link scenario (the index ℓ is dropped), b) attenuation [dB] across the LOS path (*i.e.,* for $x = d/2 = 2.5$ m) and c) along the LOS path ($y = 0$ m). Results from an experimental field trial with a reference target (red crosses) and from an EM simulator with PEC models are also shown for comparison. Black dots represent the results using a PEC obstacle over a concrete floor, while black crosses refer to a PEC target without considering the floor effects.

to randomly rotate with angle $0 \le \theta < 2\pi$ around the vertical axis passing through the barycenter $\mathbf{x}$. The traversal size $a_y(\theta)$ of the 3D target thus changes according to the angle θ, where the semi-size $a_y = a_y(\theta) \in [a_{yv}, a_{yu}]$ with $a_{yv} = \min_\theta[a_y(\theta)]$ and $a_{yu} = \max_\theta[a_y(\theta)]$.

The variation of path-loss and fading (2)-(3) due to the human body is here evaluated according to these random displacement and rotation effects by averaging over the

azimuth θ and the small movements $\triangle\mathbf{x}$ according to

$$\Delta\mu_\ell(\mathbf{x}) = \Delta\mu_C + \mathrm{E}_{\theta,\triangle\mathbf{x}}\left[A_C\left(\mathbf{x}+\triangle\mathbf{x}, a_y\left(\theta\right), a_z, d_\ell\right)|_{\mathrm{dB}}\right], \tag{5}$$

while the standard deviation (3) can be rewritten as

$$\Delta\sigma_\ell\left(\mathbf{x}\right) = \Delta\sigma_C + \mathrm{Std}_{\theta,\triangle\mathbf{x}}\left[A_C\left(\mathbf{x}+\triangle\mathbf{x}, a_y\left(\theta\right), a_z, d_\ell\right)|_{\mathrm{dB}}\right], \tag{6}$$

where $\Delta\mu_C$ and $\Delta\sigma_C$ include residual stochastic effects and measurement errors that are assumed constant for all links [13]. Once the maps $\{\Delta\mu_\ell(\mathbf{x}), \Delta\sigma_\ell(\mathbf{x})\}$ have been built, target localization can be obtained by maximum likelihood estimation (MLE) [13] [17].

Validation of the analytical maps (5)-(6) is carried out in Fig. 2 for a specific indoor scenario. The numerical results are compared to the model considered in [14] where simplifying assumptions have been considered for rotation and no target movements are taken into account. Figs. 2 (b), (c) show the attenuation term $\Delta\mu_\ell(\mathbf{x})$ in dB scale, across (*i.e.,* for $x = 2.5$) and along (*i.e.,* for $y = 0$) the LOS path, respectively when both rotation θ and $\triangle\mathbf{x}$ terms are included. Both target rotation and movement are assumed to be uniformly distributed as $\mathcal{U}(0, 2\pi)$ and $\mathcal{U}(-\boldsymbol{\Delta}/2, +\boldsymbol{\Delta}/2)$, respectively. Similar results can be also obtained for $\Delta\sigma_\ell(\mathbf{x})$. The target parameters used for the simulations are the same employed in [14]: $a_{yu} = 0.275$ m, $a_{yv} = 0.12$ m, $a_z = 0.9$ m, $h = 0.95$ m and $\lambda = 0.12$ m. In the same figure, the results obtained from a commercially available EM software simulator are shown as a reference where the human body is simulated as a perfect EM conductor (PEC); ground effects from a concrete floor with EM parameters $\epsilon_r = 5$ and $\tan\delta = 0.14$ are also considered.

Comparisons of the numerical results show a reasonable matching of the model-based prediction with the measurements from experimental field trials and the PEC results. The difference between analytical model and the measurements are mainly due to the 2D approximation of a generic 3D target ignoring important EM parameters such as polarization, permittivity/conductivity values, surface roughness, thickness, shape and material. It is also apparent how the random movements of the target within the spatial bin give rise to a changing attenuation with the bin size Δ. As expected, the attenuation function gets smoother for increasing Δ, as this accounts for the lower spatial resolution of practical DFL systems that average the RSS observations over a finite spatial/temporal window. The parameter Δ needs to be adjusted for the specific scenario according to the user mobility and the system sampling rate Δt (see Sect. V). For details about the experimental measurements, the interested reader can refer to [14].

IV. Accuracy Bounds for DFL Systems

In this section, the models for excess attenuation (5) and standard deviation (6) are used to predict the DFL accuracy based on the CRLB analysis. According to the log-normal model (1), the CRLB for any unbiased estimator $\hat{\mathbf{x}}$ of the target position $\mathbf{x}$ can be evaluated as

$$\mathrm{Cov}(\hat{\mathbf{x}}) = \mathrm{E}[(\mathbf{x}-\hat{\mathbf{x}})(\mathbf{x}-\hat{\mathbf{x}})^{\mathrm{T}}] \geq \mathbf{F}^{-1}(\mathbf{x})$$

where $\mathbf{F}(\mathbf{x})$ is the 2×2 Fisher information matrix (FIM). Let $\Lambda(s_{\ell,t}|\mathbf{x})$ be the likelihood for a given link according to the Gaussian model in Sect. II, using the assumption of uncorrelated link observations, the FIM is obtained as [16]

$$\mathbf{F}(\mathbf{x}) = \mathrm{E}\left[\frac{\partial\Lambda(\mathbf{s}_t|\mathbf{x})}{\partial\mathbf{x}}\frac{\partial\Lambda(\mathbf{s}_t|\mathbf{x})^T}{\partial\mathbf{x}}\right] = \sum_{\ell=1}^{L}\mathbf{F}_\ell(x) \tag{7}$$

where $\mathbf{F}_\ell(x)$ is the FIM for the ℓ-th link. It can be shown that the ℓ-th link FIM reduces to:

$$\mathbf{F}_\ell(x) = \frac{1}{\sigma_\ell^2(\mathbf{x})}\left[\mathbf{h}_\ell(\mathbf{x})\mathbf{h}_\ell^T(\mathbf{x}) + 2\mathbf{q}_\ell(\mathbf{x})\mathbf{q}_\ell^T(\mathbf{x})\right] \tag{8}$$

where $\mathbf{h}_\ell(\mathbf{x}) = \frac{\partial\mu_\ell(\mathbf{x})}{\partial\mathbf{x}} = \frac{\partial\Delta\mu_\ell(\mathbf{x})}{\partial\mathbf{x}}$ and $\mathbf{q}_\ell(\mathbf{x}) = \frac{\partial\sigma_\ell(\mathbf{x})}{\partial\mathbf{x}} = \frac{\partial\Delta\sigma_\ell(\mathbf{x})}{\partial\mathbf{x}}$ are the 2×1 Jacobians that embody the information on the target location provided by the attenuation and standard-deviation functions, respectively (constant terms related to the empty-space have no impact on the accuracy).

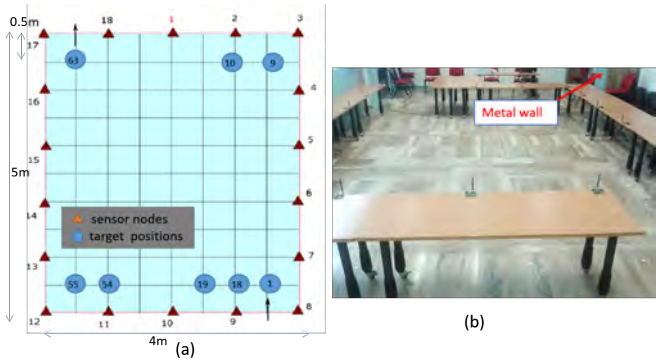

Fig. 3. Experimental scenario: (a) Scheme of the DFL layout with node positions and explored target locations, (b) Indoor environment.

V. Predictive Analysis and Validation

In this section, we assess the ability of the tool proposed in Sect. III-IV to predict the DFL performances by comparing the analytical bound with root mean square error (RMSE) values provided by a previously developed DFL prototype [13]. Experiments have been conducted in an indoor environment with $N = 18$ wireless devices, as shown in Fig. 3. Devices are equipped with a low-power single-chip 2.4 GHz transceiver conforming to the IEEE 802.15.4 standard. As shown in Fig. 3 (a), the nodes are deployed along the boundary of a 5 m $\times$ 4 m area where the target can freely move. Different network topologies will be considered in the experiments, by activating subsets of the $L = 153$ available device-to-device links based on the application-layer needs.

The DFL prototype performs online MLE location estimation based on RSS measurements collected in real-time, using the log-normal model (1) with maps $\{\Delta\widehat{\mu}_\ell(\mathbf{x}), \Delta\widehat{\sigma}_\ell\left(\mathbf{x}\right)\}$

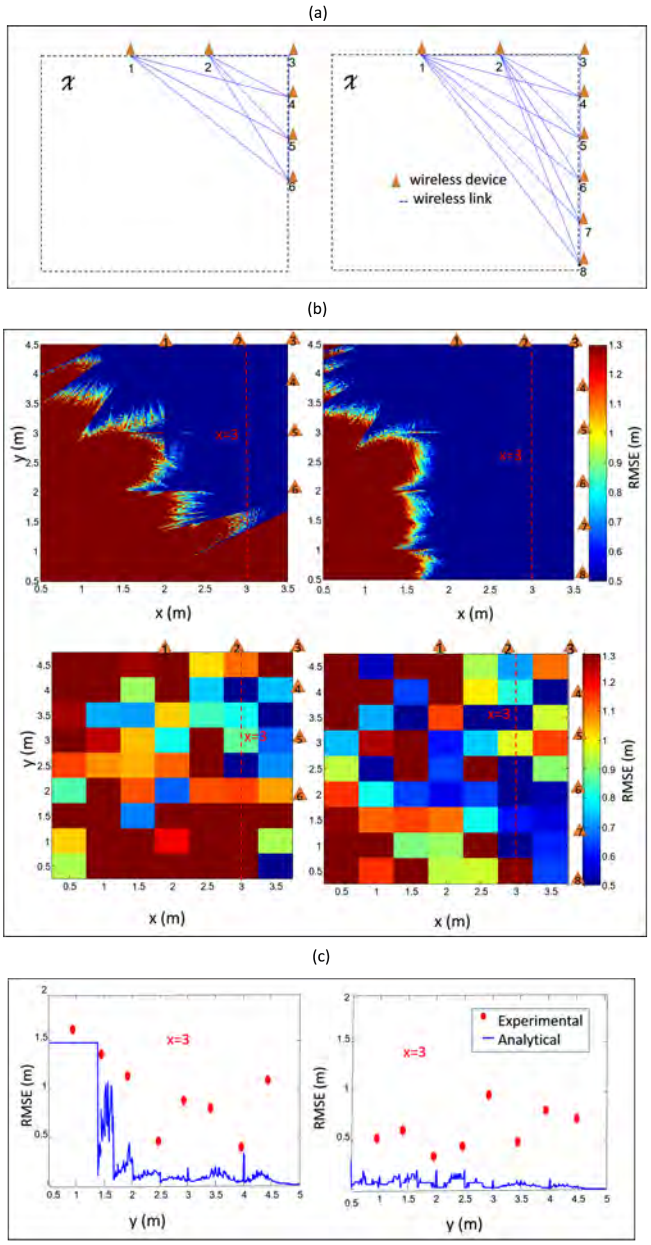

Fig. 4. Predicted accuracy and experimental validation for two node deployment topologies including nodes 1 to 6 (left) and nodes 1 to 8 (right). From top to bottom: (a) node deployment topologies; (b) analytical prediction derived from the EM model and RMSE image of the position estimation from the experimental measurements; (c) analytical prediction and experimental RMSE figures for a target moving on the line segment x=3 (predicted accuracy is saturated for visualization purposes).

built during a pre-calibration phase [13]. The maps are obtained, using a fingerprinting approach, by collecting RSS fingerprints over 63 different target positions as highlighted in Fig. 3 (a). Note that these maps are ad-hoc built for the considered scenario and might differ from the predicted ones in (5)-(6), as they also account for multipath effects that are not considered in the diffraction-based model. The practical impact of these model deviations on pre-

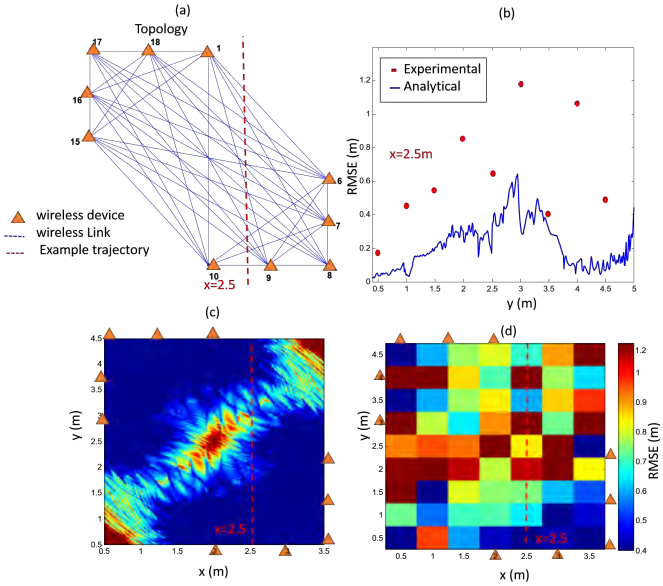

Fig. 5. Predicted accuracy and experimental validation for the network deployment that includes nodes 1, 6-10 and 15-18. (a) Sensor deployment; (b) experimental RMSE and predicted accuracy figures for a target moving along the line segment $x = 2.5$; (c) predicted accuracy image from the analytical model; (d) RMSE position estimation image from the experimental measurements.

deployment accuracy assessment will be addressed in the following comparative analysis. In the online phase of the DFL experiments, the target moves over a trajectory that covers all the 63 locations highlighted in Fig. 3 (a) with an average velocity of $v = 0.5$ m/s. Location estimation is performed every $\triangle t = 360$ ms by combining the likelihoods of 6 time-consecutive RSS samples for each link. Position deviation $\Delta \mathbf{x}$ for predictive analysis is accordingly set to $\triangle \mathbf{x} = 0.18$ m. For the analytical tool, the model parameters tuned on real RSS data are as follows: $\sigma_{\ell,0} = 1.4$ dB for the log-normal model in (1), $\Delta\mu_C = 0$ dB and $\Delta\sigma_C = 2$ dB for the diffraction-based model of (5)-(6).

Fig. 4 shows the location accuracy predicted by the analytical tool compared to the one measured by the DFL prototype for two different network topologies. The two layouts are in Fig. 4 (a): the first one (left) consists of 6 nodes (1 to 6), while the second one (right) includes 2 additional nodes (1 to 8). Fig. 4 (b) shows the location accuracy as predicted by the analytical model over the whole square area vs. the accuracy measured by the DFL prototype. The numerical results highlight the effect of node density increase on the DFL accuracy. As expected, both analytical and experimental results confirm that the deployment with 8 nodes (right sub-figures) provides improved localization performance and increased area coverage, particularly in the area surrounding the additional devices (*i.e.,* nodes 7 and 8). Also, Fig. 4 (c) shows the analytical and experimental localization performance for a target moving along the line segment $x = 3$ m. Note that in both cases the proposed

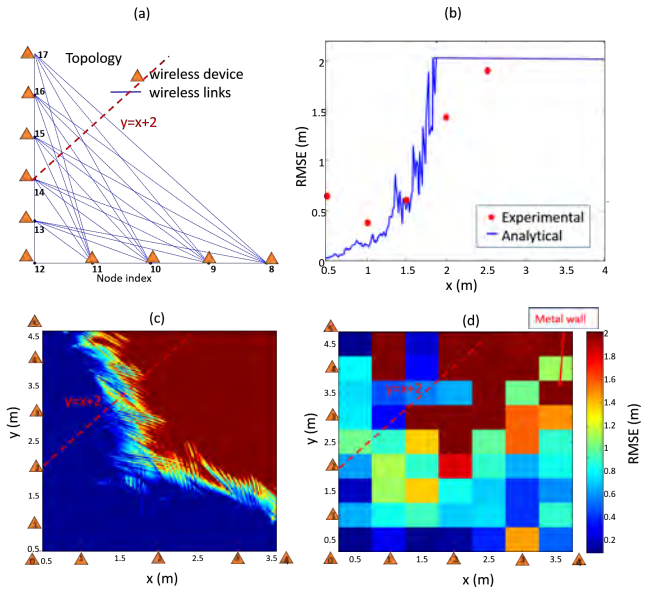

Fig. 6. Predicted accuracy and experimental validation for the network deployment that includes nodes 8-17. (a) Sensor deployment; (b) experimental vs. predicted accuracy figures for a target moving along the section $y = x+2$; (c) predicted accuracy for a target located inside the layout area; (d) RMSE position estimation image from the experimental measurements.

analytical tool can reasonably predict the DFL performance also in the boundary of the area which exhibits marginal coverage (*e.g.,* see the saturated performance for $y < 1.4$ m in the left plot of Fig. 4 (c)).

Additional network topologies are considered in Figs. 5 and 6. For the network layout of Fig. 5 (a), the plot in Fig. 5 (b) gives the predicted and experimental localization performances along the section $x = 2.5$ m. As shown by the analytical results in Fig. 5 (c) and the experimental ones in Fig. 5 (d), the localization error increases up to 0.6 m and 1.2 m, respectively, when the target gets close to the center of the monitored area, as this region is covered by only few links with reduced sensitivity according to the diffraction model. Moreover, the shape of the zone with degraded performances is almost symmetric with respect to the main diagonal.

In Fig. 6, 10 nodes with all-to-all connectivity are considered around the lower diagonal area of the network topology of Fig. 6 (a). Localization performances (both analytical and experimental) are evaluated along the line segment $y = x + 2$ in Fig. 6 (b) and over the whole area in Fig. 6 (c)-(d). The accuracy is good in the bottom-left region of the monitored area (*e.g.,* the location error is below 0.5 m), while it worsen in the top-righ region not covered by the links (*e.g.,* the location error is above 1.7 m) where the predicted performance saturates to approximately 2 m.

Despite some model mismatches, possibly caused by the multipath effects observed in the indoor environment (*e.g.,* in proximity to the walls as shown in Fig. 6 (d)) that are not considered by the diffraction model, the experimental results confirm the predicted model behavior in all considered network deployments. We can thus conclude that the analytical tool provides an effective prediction of the DFL system performances and reasonable enough for pre-deployment assessment.

VI. Concluding Remarks

In this paper, we proposed a novel tool for pre-deployment prediction of DFL accuracy. The model is general enough to be applied to DFL systems with any kind of network topology and connectivity. The tool has been corroborated by extensive experimental activity considering regular/non-regular network layouts. Post-deployment localization accuracy has been also verified based on a DFL implementation. Future developments will be focused on deployment optimization.

References

[1] S. Savazzi et al., "Device-free radio vision for assisted living: Leveraging wireless channel quality information for human sensing," *IEEE Signal Processing Magazine*, vol. 33, no. 2, pp. 45-58, Mar. 2016.

[2] M. Youssef et al., "Challenges: device-free passive localization for wireless environments," *Proc. of the 13th annual ACM International Conference on Mobile Computing and Networking,* pp. 222-229, 2007.

[3] N. Patwari et al., "RF sensor networks for device-free localization: Measurements, models, and algorithms," *Proc. of the IEEE*, vol. 98, no. 11, pp. 1961–1973, Nov. 2010.

[4] S. Savazzi et al., "Device-free human sensing and localization in collaborative human-robot workspaces: a case study," *IEEE Sensors Journal,* vol. 16, no. 5, pp. 1253-1264, Mar. 2016.

[5] S. Kianoush et al., "Leveraging RF signals for human sensing: fall detection and localization in human-machine shared workspaces," *Proc. of IEEE conference on industrial informatics (INDIN'15)*, pp. 1456-1462, Jul. 2015.

[6] L. Yao et al., "Exploring tag-free RFID-based passive localization and tracking via learning-based probabilistic approaches," *Proc. of the 23rd ACM Intl. Conference on Information and Knowledge Management (CIKM)*, Shanghai, China, 2014.

[7] A. Saeed et al., "A low-overhead robust WLAN device-free passive localization system," *IEEE J. Sel. Topics in Signal Proc.*, vol. 8, no.1, pp. 5-15, Feb. 2014.

[8] J. Wilson et al., "Radio tomographic imaging with wireless networks," *IEEE Trans. on Mobile Comp.*, vol. 9, no. 5, pp. 621-632, 2010.

[9] Y. Mostofi et al., "Cooperative wireless-based obstacle/object mapping and see-through capabilities in robotic networks," *IEEE Trans. on Mobile Computing*, vol. 12, no. 5, May 2013.

[10] G. Koutitas et al., "Multiple human effects in body area networks," *IEEE Antennas and Wireless Propagation Letters*, vol. 9, pp. 938-941, Sept. 2010.

[11] M. Scholz et al., "Device-free radio-based low overhead identification of subject classes," *Proc. of 2nd Workshop on Physical Analytics (WPA15)*, pp. 1-6, May 2015.

[12] D.B. Smith et al., "Propagation models for body-area networks: a survey and new outlook," *IEEE Antennas and Propagation Mag*, vol. 55. no. 5, pp. 97-117, Oct. 2013.

[13] S. Savazzi et al., "A Bayesian approach to Device-Free Localization: modeling and experimental assessment," *IEEE Journal on Sel. Topics in Signal Proc.*, vol. 8, no. 1, pp. 16-29, Feb. 2014.

[14] V. Rampa et al., "Physical Modeling and Performance Bounds for Device-free Localization Systems," *IEEE Signal Processing Letters*, vol. 22, no. 11, pp. 1864-1868, Nov. 2015.

[15] A.J. Coulson et al., "A statistical basis for lognormal shadowing effects in multipath fading channels," *IEEE Trans. on Communications*, pp. 494-502, 1998.

[16] S. Kay, *Fundamentals of Statistical Signal Processing: Estimation Theory.* Prentice Hall, 1993.

[17] K. Xinghong et al., "Maximum likelihood localization algorithm using wireless sensor networks," *Proc. of IEEE International Conference on Innovative Computing, Information and control*, pp. 263-266, Aug. 2006.